Structure and water uptake in $BaLnCo_2O_{6-\delta}$ (Ln =La, Pr, Nd, Sm, Gd, Tb and Dy)

Sebastian Lech Wachowski[1*], Iga Szpunar[1], Magnus Helgerud Sørby[2], Aleksandra Mielewczyk–Gryń[1], María Balaguer[3], Corneliu Ghica[4], Marian Cosmin Istrate[4], Maria Gazda[1], Anette E. Gunnæs[5], José M Serra[3], Truls Norby[6], and Ragnar Strandbakke[6]

[1] Department of Solid State Physics, Faculty of Applied Physics and Mathematics, Gdańsk University of Technology, ul. G. Narutowicza 11/12, 80-233 Gdańsk, Poland

[2] Institute for Energy Technology, Department for Neutron Materials Characterization, P.O. Box 40, 2027 Kjeller, Norway

[3] Instituto de Tecnología Química, Universitat Politècnica de València - Consejo Superior de Investigaciones Científicas, av. Los Naranjos sn, 46022 Valencia, Spain

[4] National Institute of Materials Physics, Atomistilor Street, no. 405 A, 077125, Magurele, Romania

[5] Department of Physics, Centre for Materials Science and Nanotechnology, University of Oslo, FERMiO, Gaustadalléen 21, NO-0349 Oslo, Norway

[6] Department of Chemistry, Centre for Materials Science and Nanotechnology, University of Oslo, FERMiO, Gaustadalléen 21, NO-0349 Oslo, Norway

*corresponding author: sebastian.wachowski@pg.edu.pl, Address: Centrum Nanotechnologii A, Gdańsk University of Technology, ul. G. Naturowicza 11/12, 80-233 Gdańsk, Poland

Keywords:

Fuel cell materials, Neutron Diffraction, X-ray synchrotron radiation, TEM, Positrode

Abstract

The structure of $BaLnCo_2O_{6-\delta}$ (Ln =La, Pr, Nd, Sm, Gd, Tb and Dy) was studied by the means of synchrotron radiation powder X-ray diffraction, neutron powder diffraction and Transmission Electron Microscopy (TEM), while water uptake properties were analysed with the use of thermogravimetry (TG) and water adsorption isotherms. The structure refinement revealed that the dominant phase in all compositions was orthorhombic with an ordering of the A-site cations along the c-axis and ordering of oxygen vacancies along the b-axis, which was also directly evidenced by TEM. It was shown that both unit cell volume and average Co-oxidation state at room temperature decrease linearly with decreasing Ln radius. TG water uptake experiments in humidified N_2-O_2 gas mixture at 300°C revealed that among all compositions, only $BaLaCo_2O_{6-\delta}$ and $BaGdCo_2O_{6-\delta}$ exhibit significant water uptake. Surface water adsorption studies showed that the α, a normalised parameter reflecting the surface hydrophilicity, mostly independently of Ln radius was close to 0.5, which means that the surface is neither hydrophobic nor hydrophilic. The results indicated that water uptake observed at 300 °C is a bulk process, which cannot be described by standard hydration/hydrogenation reaction and it is related to the layered structure of the perovskite lattice and characteristic to La or Gd being present in the lattice.

1. Introduction

Double perovskite barium lanthanide cobaltites, $A^IA^{II}Co_2O_{6-\delta}$, where A^I stands for Ba and A^{II} for lanthanide (BLnCOs) and their derivatives are components in electrochemical and electrocatalytic devices [1–9]. It has been shown that these materials adopt multiple polymorphs, most commonly cubic (space group $Pm\bar{3}m$, no 221) [1,10], and A-site ordered tetragonal (P4/mmm no 123, double c-axis) or orthorhombic (Pmmm no 47, double b- and c-axis) structures [1,11]. Furthermore, a variety of possible superstructures (e.g. with tripled unit cells along a- and b-axes) [12,13] and domains [14] have been reported. The cubic symmetry implies disordering of Ba and Ln over the same crystallographic site and the formula unit is thus written as $Ba_{0.5}Ln_{0.5}CoO_3$, while $BaLnCo_2O_{6-\delta}$ represents the layered structure with Ba and Ln on alternating A-sites along the c-axis, in which the unit cell is doubled [4].

The high electronic conductivity of BLnCOs combined with their high oxide ion mobility at elevated temperatures (>300°C) in oxidizing conditions [15] makes them good examples of ceramic mixed ionic-electronic conductors (MIECs), well suited as electrode materials in high temperature electrochemical cells [1–3,7,8,16,17]. Furthermore, the possible presence of protonic defects reported in literature makes this materials class interesting as positrodes (positive electrodes [16]) in Proton Ceramic Electrochemical Cells (PCECs) or Proton Ceramic Fuel Cells (PCFCs) [2,3,17]. The proclivity of Co to adopt different spins and oxidation states confers high electro-catalytic activity and allows that the double perovskite structure in $BaLnCo_2O_{6-\delta}$ is formed for many different lanthanides [16,18]. Moreover, the structure can sustain large oxygen non-stoichiometry, to the point where the Ln-O layers are essentially vacant on all oxygen sites [11,19,20]. This paper addresses the possible relation between structure, oxygen non-stoichiometry and hydration in the $BaLnCo_2O_{6-\delta}$ series.

This work is a part of a larger study on the governing principles of hydration in mixed conducting double perovskite oxides [21], aiming to screen a matrix of lanthanides and d-block metals to investigate any possible effect of Ln size and electronegativity on hydration. This first part is an extensive structural study and a qualitative screening of hydration over the Ln series. This study will be followed by a new matrix of mixing different Ln's on A^{II} and substituting for Ba on A^{I}, and for Co on the B-site, following in our next publication. So far, there have been a few reports on protons in mixed conducting perovskites [2,17,22], all with a mix of four cations and all with Ba on the A-site. Many of the reported Mixed Proton and Electron Conducting Ceramics (MPECs) also bear an uncertainty with respect to quantification of the proton uptake.

The structures were characterised employing simultaneous Rietveld refinement of Synchrotron Radiation Powder X-ray Diffraction (SR-PXD) and Neutron Powder Diffraction (NPD). To support the diffraction methods, high-resolution Transmission Electron Microscopy (TEM) was performed, including conventional and High-Resolution imaging (TEM/HRTEM), Selected-Area Electron Diffraction (SAED), Scanning Transmission Electron Microscopy (STEM), Electron Energy

Loss Spectroscopy (EELS), Energy Dispersive X-ray Spectroscopy (EDS) and combined imaging-analytical techniques for chemical mapping at atomic spatial resolution (STEM-EELS-SI). The evolution of oxygen vacancy concentration as a function of temperature was studied by the means of Thermogravimetry (TG) in controlled oxygen partial pressure, and absolute stoichiometry at room temperature was found by Iodometric Titration (IT). Finally, proton uptake was studied by two techniques: TG with controlled water vapour partial pressure and water sorption studies.

2. Experimental

$BaLnCo_2O_{6-\delta}$ samples (Ln = La, Pr, Nd, Sm, Gd, Tb, Dy) were synthesised by solid state reaction. The lanthanide sources were La_2O_3 (99.99% Alfa Aesar, preheated at 900°C for 5 hrs), Pr_6O_{11} (99.99% Aldrich), Nd_2O_3 (99.9%, Chempur, preheated at 900°C for 5 hrs), Sm_2O_3 (99.9%, Chempur), Gd_2O_3 (99.98% Alfa Aesar) or Gd_2O_3 (99,7%, Trace Sciences International), Tb_4O_7 (99.99% Aldrich) and Dy_2O_3 (99.9%, Chempur). The stoichiometric amounts of $BaCO_3$ (99.9% Sigma Aldrich), Co_3O_4 (99.98% Alfa Aesar) and a binary oxide of the lanthanide were mixed in an agate mortar and pelletized. The green bodies were annealed in static air at 1150°C for 48 h. To form the tetragonal $BaLaCo_2O_{6-\delta}$, the as-synthesised sample was annealed in Ar flow at 1050°C for 24 h and in air flow at 350°C for 3 h.

Powder X-ray Diffraction (PXD) was used for initial phase identification. X-ray diffractograms were collected in 2θ angle from 20° to 80° with a Phillips X'Pert Pro diffractometer with Cu K_α radiation, proportional counter, and Bragg-Brentano geometry. Further structure studies were performed by Synchrotron Radiation Powder X-ray Diffraction (SR-PXD) and Powder Neutron Diffraction (PND).

SR-PXD patterns were obtained at the Swiss-Norwegian Beamline (SNBL) BM01 [23] and BM31 [24], ESRF, Grenoble with a Pilatus 2M 2-dimensional (2D) detector (BM01) and Dexela-Perkin Elmer 2923 CMOS 2D detector (BM31) with wavelengths of 0.78956 Å and 0.31232 Å, respectively. 1D data were obtained by integration of the 2D diffraction patterns using the program Bubble [23]. Additional SR-PXD measurements were performed at beam line I11 at the Diamond Light Source in Didcot, U.K. Data were collected in high-resolution mode

by 45 photomultiplier detectors, each with a Si(111) analyser crystal [25] (λ = 0.82657 Å). The samples were contained in 0.3 mm borosilicate capillaries.

For the PND experiments, the compositions with Sm and Dy were excluded due to the strong neutron absorption of these elements. Natural Gd is also prohibitively absorbing due to the extreme neutron absorption cross section of some of the isotopes, especially ^{155}Gd and ^{157}Gd. For PND and SR-PXD, a ^{160}Gd isotope enriched sample ($Ba^{160}GdCo_2O_{6-\delta}$) was therefore synthesised, containing only 0.20 and 0.26 %, respectively, of the absorbing isotopes, what, in comparison to the natural abundance of gadolinium isotopes equal to 14.8% and 15.65% for ^{155}Gd and ^{157}Gd, respectively, is a significantly reduced value. The synthesis protocol of the ^{160}Gd isotope sample was the same as for the other compositions, except for a slightly higher annealing temperature of 1200°C.

PND data were collected at RT using the constant-wavelength diffractometer PUS (λ =1.555 Å) at the JEEP II reactor (Kjeller, Norway) [26] and the time-of-flight (TOF-PND) instrument POWGEN at SNS (Oak Ridge, UK) [27]. The sample was loaded in vanadium cans with a diameter of 6 mm (PUS) or 3 mm (POWGEN). The results were analysed using the Rietveld method [28] with the Topas Academic 6 software from Alan Coelho [29].

The structure models were refined simultaneously to the SR-PXD and PND data, when available. The datasets were weighted so that they contributed equally to the overall agreement factors (R_{wp} and χ^2). The constant-wavelength peak shapes were described by Thomson-Cox-Hasting pseudo-Voigt functions with four refined parameters. The time-of-flight peak shapes were described by back-to-back exponentials convoluted with a pseudo-Voigt function with 7 refined parameters. The backgrounds were modelled with Chebyshev polynomials with up to 30 terms. The displacement parameters (B_{iso}) used to fit the SR-PXD pattern could differ from those refined from the PND data since they correlated strongly with the X-ray absorption. During the refinement, all the three symmetries, i.e. cubic $Pm\bar{3}m$, tetragonal $P4/mmm$ and orthorhombic $Pmmm$, were considered. More details about the experimental procedures and the refinement are given in the Supplementary

Information (SI). In all cases, to visualise the refined structures, Vesta software [30] was used.

The microstructure was investigated with the use of a FEI Quanta FEG 250 Scanning Electron Microscope (SEM). The imaging was performed with secondary electron Everhart-Thornley Detector (ETD) and Backscattered Electrons Detector (BSED). The samples' specific surface area was determined by standard 10-points BET measurements using Quantachrome iQ Autosorb apparatus.

Transmission electron microscopy (TEM) measurements were performed on powders of $BaLnCo_2O_{6-\delta}$, where Ln = La, Pr, Nd or Gd. The samples were prepared by grinding in a mortar followed by dripping on a TEM grid. The analytical TEM investigations were performed on a probe-corrected JEM ARM 200F instrument provided with Energy Dispersive X-ray Spectroscopy (EDS) and Electron Energy Loss Spectroscopy (EELS) analytical units. For the identification of possible superstructures determined by ordering processes, several TEM techniques were used including conventional and High-Resolution imaging (TEM/HRTEM), Selected-Area Electron Diffraction (SAED), Scanning Transmission Electron Microscopy (STEM), EELS, EDS and combined imaging-analytical techniques for chemical mapping at atomic spatial resolution (STEM-EELS-SI). For the digital processing and signal-to-noise ratio (SNR) enhancement of the EEL Spectrum Images, we used the temDM MSA routine running under Digital Micrograph [31]. For the simulation of the HRTEM patterns, the multislice technique was used, with the use of Crystal Kit and Mac Tempas software kits. In each case, series of simulated images were generated according to the sample thickness t and the defocus of the objective lens, Δf.

Iodometric titration was used to study the oxidation state of cobalt and oxygen non-stoichiometry. 15-20 mg of the sample and a surplus of potassium iodide (ca. 0.2 g) were put in a three-neck flask, flushed with nitrogen. When the air was removed, 15 ml of 2 M HCl was added to dissolve the sample. The iodine ions were titrated in an inert atmosphere with 0.01 mol/dm^3 $Na_2S_2O_3$ using 10 ml microburette (±0.05 ml) and starch was used as an indicator.

The thermogravimetric oxidation studies were performed in synthetic air as purge gas (with N_2 as protective gas) atmosphere using a Netzsch Tarsus 401 thermobalance in the temperature range RT-900°C, with a temperature step of 2°/min on both cooling and heating. Hydration studies were performed using a Netzsch Jupiter® 449 F1 thermal analyser. The as-prepared powders were heated to 800°C (5°/min) and held at this temperature for 5 h under dry atmosphere After drying, the samples were cooled to 300°C in dry gas (5°/min). After 2 hours of stabilisation, the dry purge gas was switched to the humidified gas, then after an additional 2 h, the purge gas was switched back to the dry gas. Nitrogen was used as a protective gas through the measurement. The water partial pressure for the humid condition was set as pH_2O=0.01 atm.

Room temperature water vapour sorption studies were undertaken on a Quantachrome iQ Autosorb apparatus in the relative pressure range p/p0 from 0.05 to 0.9. Before measurements, samples were degassed at 300°C in a vacuum.

3. Results

Structural analysis

Figure 1 presents unit cells of the three most common polymorphs of the studied material: disordered cubic perovskite and ordered tetragonal and orthorhombic double perovskites. The A-site cations (Ln and Ba) in the tetragonal and orthorhombic phases form Ln-O and Ba-O alternating layers in the ab plane, separated by Co-O layers, leading to a doubling of the c-parameter. The oxygen sites in the barium, cobalt and lanthanide layers will here be denoted as O1, O2 and O3, respectively. The difference between the two double perovskite polymorphs can be found both in the anion and cation sub-lattices. In the tetragonal polymorph, there is only one oxygen site in the Ln-O layer, denoted as O3 in this paper. In the orthorhombic phase, there are two oxygen sites in the Ln layer, denoted here as O3a and O3b (labelled in Figure 1c), with distinctly different occupancies. The O3a occupancy is usually close to 1, while O3b contains most of the oxygen vacancies and can have occupancy equal to zero. This leads to a doubling of the b-parameter compared to the cubic and tetragonal polymorphs. The lowered symmetry is also observed in oxygen positions in the Ba-O and Co-O

planes, denoted as O1a, O1b and O2a, O2b, O2c, respectively. In the orthorhombic cation sub-lattice, the Co position next to O3b (denoted now as Co2) moves away (in c direction) from the oxygen site as the attractive force between metal cations and oxygen anions is reduced, due to lower occupancy of the latter. Simultaneously, the other Co position (Co1) is closer to the occupied O3a site and moves closer to the Ln-O plane. As a result, the Co cations in the lattice are stacked in a zig-zag manner along the b-axis in orthorhombic symmetry.

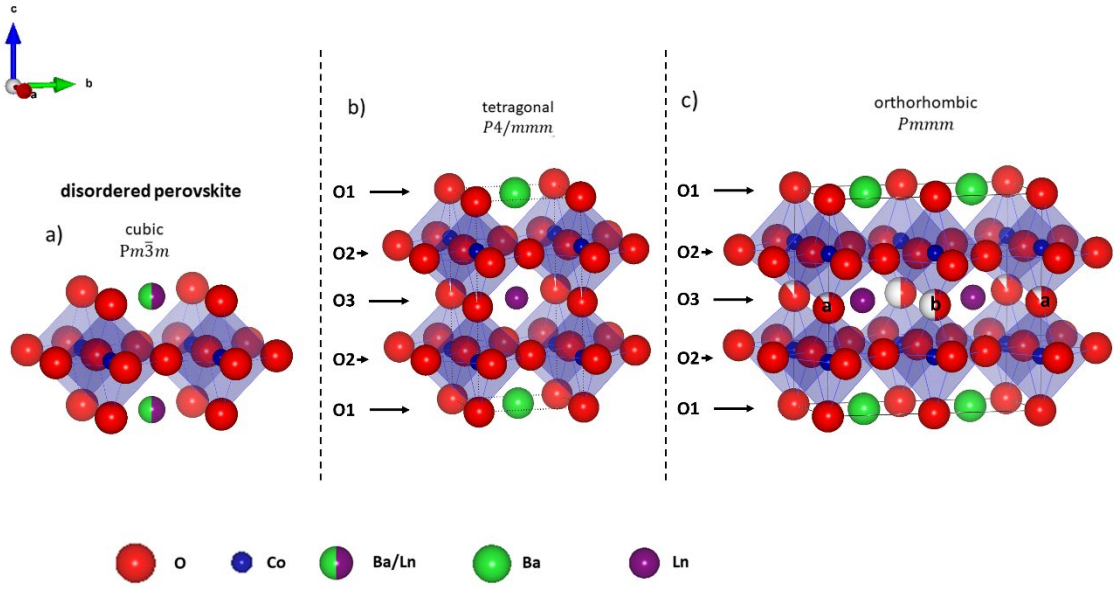

Figure 1. Examples of unit cells of (a) single perovskite cubic $Pm\bar{3}m$, (b) double perovskite tetragonal P4/mmm and (c) double perovskite orthorhombic Pmmm structure. Note that different origin choices are used in the figures compared to the structure tables S2-S8 to ease the visual comparison.

The compositional series $BaLnCo_2O_{6-\delta}$ was investigated by PXD (Figure 2). In all diffractograms, except that of barium lanthanum cobaltite, the Bragg peaks were consistent with a double perovskite structure with lattice parameter doubling along the c-axis, a signature of A-site ordering. No secondary phases were observed.

As shown in Figure 2.a, the as-synthesised La-composition has a cubic perovskite structure with disordered A-site sub-lattice. Subsequent annealing of the cubic $Ba_{0.5}La_{0.5}CoO_{3-\delta}$ in Ar at 1050°C results in A-site ordering and a doubling of the c lattice parameter which is evident from the splitting of the peaks around 32.5° and 58.5°. Figure 2.b shows the diffraction patterns for the remaining $BaLnCo_2O_{6-\delta}$ compositions. In these compositions the size difference between Ln and Ba is

larger, thus the deviation from cubic symmetry increases and the separation of peaks is more pronounced.

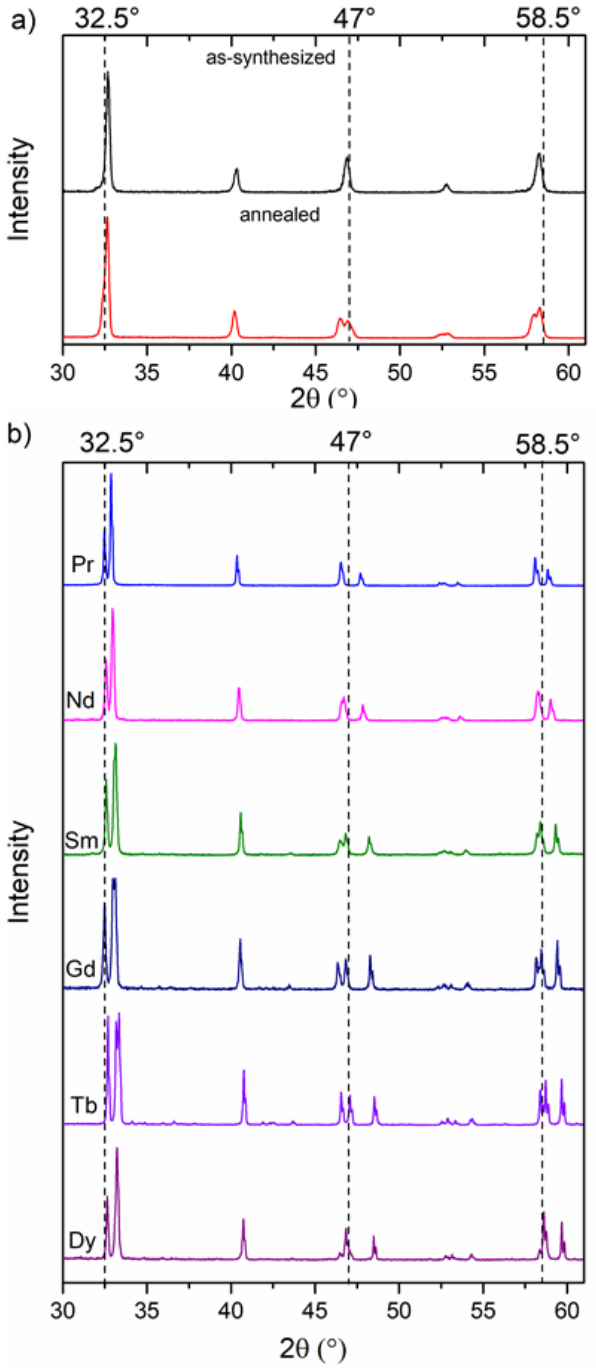

Figure 2. X-ray diffractograms of (a) pre- and post-annealed $BaLaCo_2O_{6-\delta}$ and (b) as-synthesised $BaLnCo_2O_{6-\delta}$ (Ln = Pr, Nd, Sm, Gd, Tb, Dy). The dotted lines are guides to the eye and mark the approximate positions of the peaks from cubic phase with Ln = La.

An example of a SR-PXD and PND results with refined patterns and difference plots is presented in Figure 3 for $BaPrCo_2O_{6-\delta}$. The other diffractograms and refinements are available in supplementary information (*cf.* Figures S1-S6). A general overview of crystal symmetry, unit cell parameters and quality of fit of PND and SR-PXD data have been summarised in Table 1, whilst the atomic coordinates, B_{iso} and other refined parameters are given in SI in Tables S2-S8. As it can be ascertained from the table, the structure varies from cubic perovskite to tetragonal and orthorhombic layered perovskite. Whenever possible, PND and SR-PXD data were refined simultaneously. $BaSmCo_2O_{6-\delta}$ and $BaDyCo_2O_{6-\delta}$ are the only compositions where the structure analysis relies on SR-PXD data alone due to the high neutron absorption cross-section of these lanthanides.

Table 1. Summary of PND and SR-PXD studies: symmetry, unit cell parameters and quality of refinement.

Ln	Symmetry	Unit cell parameters	R_{wp}	Comment
La*	cubic $Pm\bar{3}m$	a = 3.8850(6) Å	R_{wp}(SR-PXD) = 5.23% R_{wp}(PND) = 4.22% R_{wp}(total) = 4.71%	*As-prepared powder Data from [10]
La**	tetragonal $P4/mmm$ (35 wt. %)	a = 3.87672(8) Å c = 7.7819(3) Å	R_{wp}(SR-PXD) = 5.82% R_{wp}(PND) = 5.41% R_{wp}(total) = 5.60%	**Annealed in Ar
	orthorhombic $Pmmm$ (65 wt. %)	a = 3.9155(2) Å b = 7.8142(5) Å c = 7.7247(3) Å		
Pr	orthorhombic $Pmmm$	a = 3.864(2) Å b = 7.716(3) Å c = 7.541(3) Å	R_{wp}(SR-PXD) = 7.94% R_{wp}(PND) = 4.75% R_{wp}(total) = 6.23%	Unit cell parameters reported for PND data
Nd	orthorhombic $Pmmm$	a = 3.9090(1) Å b = 7.8050(2) Å c = 7.6163(1) Å	R_{wp}(SR-PXD) = 6.90% R_{wp}(PND) = 4.47% R_{wp}(total) = 5.50%	Unit cell parameters reported for PND data since SR-PXD data were collected at slightly elevated temperature (~90°C).
Sm	tetragonal $P4/mmm$ (25 wt. %)	a = 3.8962(1) Å c = 7.5757(4) Å	Rwp = 7.83%	PND not possible
	orthorhombic $Pmmm$ (75 wt. %)	a = 3.88795(7) Å b = 7.8375(2) Å c = 7.5603(1) Å		
Gd	orthorhombic $Pmmm$	a = 3.87707(1) Å b = 7.82650(2) Å c = 7.53379(1) Å	R_{wp}(SR-PXD) = 11.85% R_{wp}(PND) = 1.45% R_{wp}(total) = 4.19%	Subtle anisotropic line broadening in SR-PXD corrected by an 8 term spherical harmonics functions
Tb	orthorhombic $Pmmm$	a = 3.8667(2) Å b = 7.81256(5) Å c = 7.51259(5) Å	R_{wp}(SR-PXD) = 4.97% R_{wp}(PND) = 5.49% R_{wp}(total) = 4.96%	SR-PXD data contained a few minor peaks due to impurity phases. Identified impurities were: Co_3O_4 (1.17(7) wt. %); $TbCoO_3$ (1.04(4) wt. %); $CoYbO_3$ (0.38(3) wt. %)
Dy	orthorhombic $Pmmm$	a = 3.86090(5) Å b = 7.80014(11) Å c = 7.5020(1) Å	R_{wp} = 7.62%	PND not possible

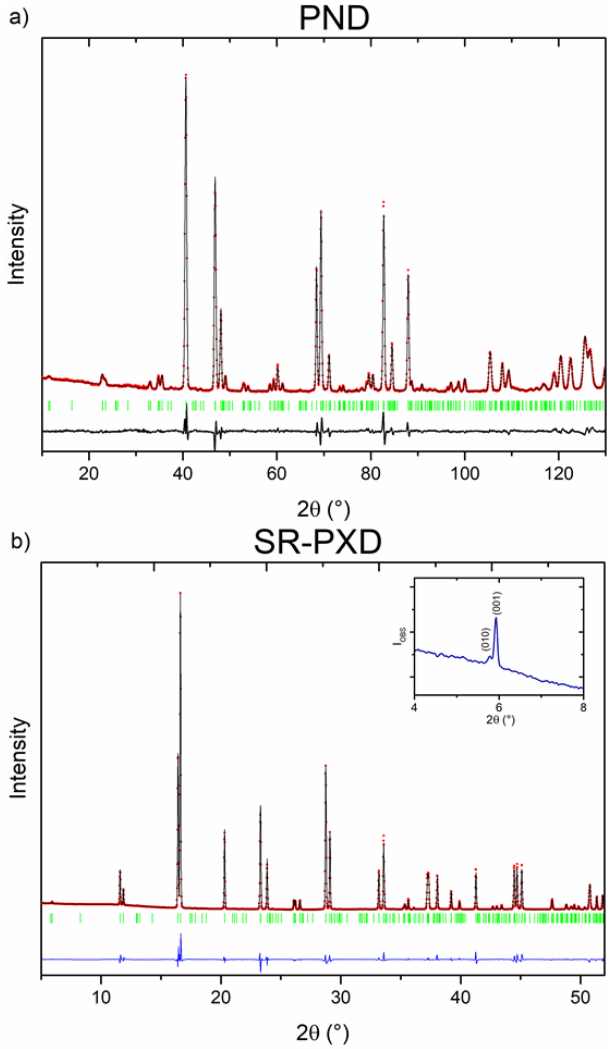

Figure 3. Diffractograms and Rietveld refinements of (a) PND and (b) SR-PXD for $BaPrCo_2O_{6-\delta}$. In the main part of each plot points represent the data, line represents fit, ticks in the middle indicate Braggs positions and the lower line is a difference plot.

The as-prepared $Ba_{0.5}La_{0.5}CoO_3$ has been a subject of our previous study [10], however, we use it in this study as reference material. The refinement of $Ba_{0.5}La_{0.5}CoO_3$ structure has shown cubic perovskite with unit cell parameter a = 3.88632(6) Å. For Ar-annealed $BaLaCo_2O_{6-\delta}$ the PND and SR-PXD Bragg-reflections indicated a tetragonal double perovskite. However, Rietveld refinements with a single tetragonal phase showed intensity mismatches between the observed and calculated data. The mismatch was not rectified by imposing a single 1x2x2 orthorhombic phase refinement but refining to a combination of tetragonal and orthorhombic phase gave an excellent fit to both the SR-PXD and the PND data. The refined phase fractions are 35.6(4) wt.% tetragonal and 64.4(4) wt.% orthorhombic perovskite. There is a high degree of overlap between the Bragg peaks from the two phases in both datasets, leading to strong correlations between other refined parameters such as atomic coordinates, occupancies and displacement parameters, which are reported in SI Tables S2-S3.

For the other compositions, namely $BaPrCo_2O_{6-\delta}$, $BaNdCo_2O_{6-\delta}$, $BaSmCo_2O_{6-\delta}$, $Ba^{160}GdCo_2O_{6-\delta}$, $BaTbCo_2O_{6-\delta}$ and $BaDyCo_2O_{6-\delta}$, the SR-PXD data show clearly

defined peaks from 1x2x2 orthorhombic superstructure, which may be seen especially in the low angle ($2\theta < 10°$) region of the diffractogram (inset in the Figure 3b), where peaks for ordering along the b-axis are observed. Therefore, most of the double perovskites were refined with a single-phase orthorhombic perovskite structure, however during the structural analysis of $BaSmCo_2O_{6-\delta}$ Rietveld refinements with a single 1x2x2 superstructure (space group *Pmmm*) gave significant intensity misfits in the strongest Bragg peaks (120, 022 and 102). The fit was improved by including a tetragonal double perovskite (1x1x2, space group *P*4/*mmm*) in the refinement. The refinements indicate close to full occupancy for the oxygen sites (O3a) in the Sm-O-layer and small occupancy of the other O-site (O3b) in the same layer, resulting in a pronounced orthorhombic distortion. The refinement shows that the material consists of around 75% orthorhombic 1x2x2 phase and 25% tetragonal double perovskite. In $BaTbCo_2O_{6-\delta}$, minor Ba-free impurity phases (< 2.5 wt. %) were detected in the synchrotron measurement, indicating a slight Ba under-stoichiometry.

For the isotope enriched $Ba^{160}GdCo_2O_{6-\delta}$, SR-PXD data reveal a single-phase 1x2x2 orthorhombic double-perovskite and Rietveld refinements were carried out with TOF-PND and SR-PXD data simultaneously, where only the B_{iso} could differ. The fitting revealed slightly anisotropic profile shapes with subtly sharper Bragg peaks for Miller indices h = k. This was mended with two spherical harmonics of 8^{th} order: one for the Gaussian and one for the Lorentzian component. The refined unit cell parameters are given in Table 1 and the refined structure data in SI Table S6.

The overall characteristic of the system is that it forms a cubic perovskite structure for Ln = La and layered perovskite structure for higher lanthanides. All studied compounds which exhibit double perovskite structure were orthorhombic and single-phase with two exceptions (Ln = La or Sm) where the tetragonal polymorph is present as a minority phase. The unit cell parameters of all compounds as a function of the lanthanide radius, R_{Ln}, are presented in Figure 4. In the figure, the unit cell parameters of cubic $Ba_{0.5}La_{0.5}CoO_3$ have been added as a reference and is represented in the figure by triangles. Note that $BaLaCo_2O_{6-\delta}$ and $BaSmCo_2O_{6-\delta}$

are two-phase systems and each of them is represented in the figure by two points with the space groups indicated next to them.

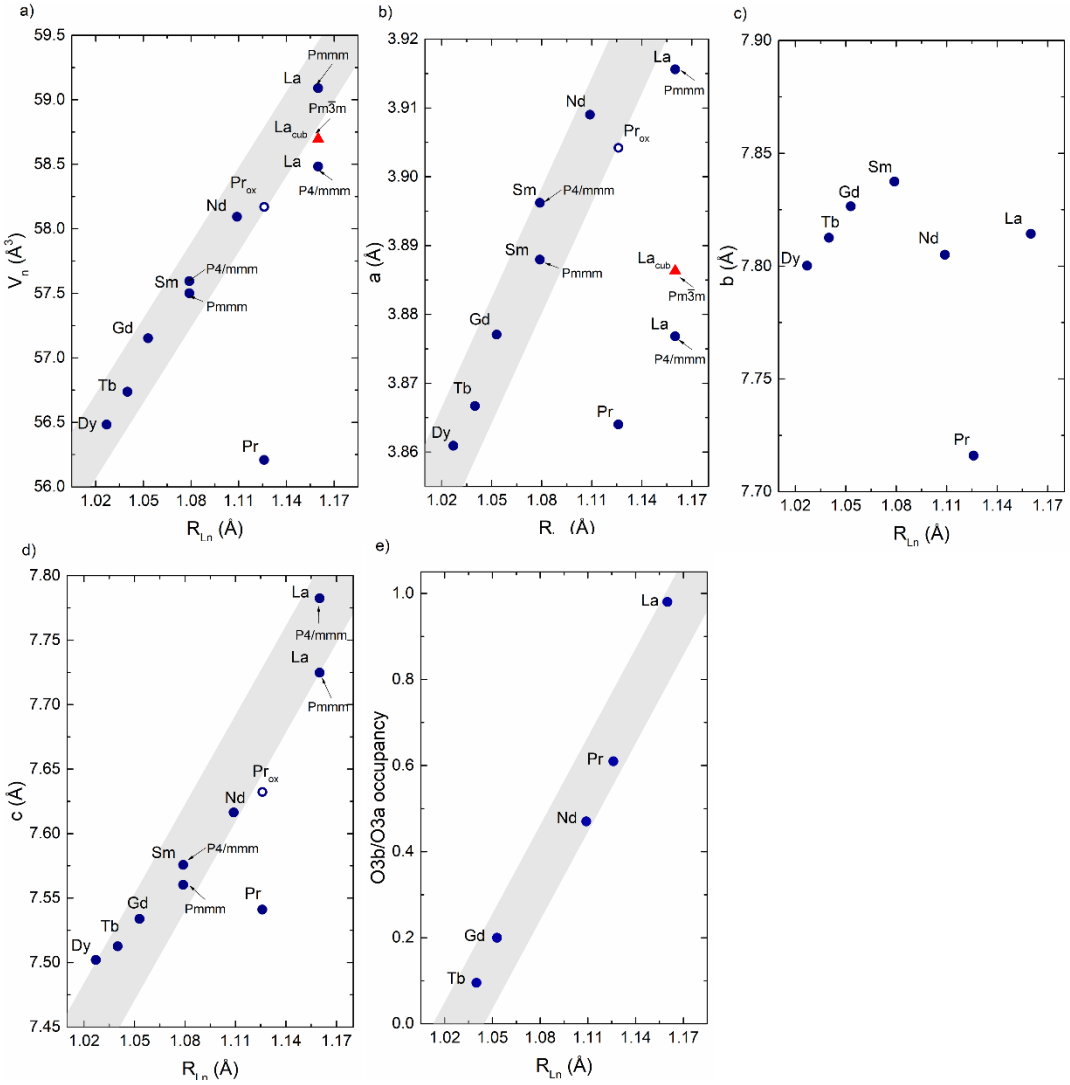

Figure 4. Selected parameters obtained from refinement of $BaLnCo_2O_{6-\delta}$ plotted as a function of Ln radius: (a) volume per formula unit, (b) a, (c) b, (d) c unit cell parameters and (e) O3b/O3a oxygen site occupancy ratio. The b parameter is plotted only for orthorhombic structure, while all the other plots are for tetragonal and orthorhombic polymorphs. The volume and a unit cell parameter for cubic $Ba_{0.5}La_{0.5}CoO_3$ have been included in (a) and (b) as a reference and is represented by triangles [10]. *The occupancy ratio is derived from PND data and given only for orthorhombic phase of $BaLnCo_2O_{6-\delta}$.* The shadow bar is a guideline to visualise the trend, not an actual fit. *The Pr_{ox} symbol denotes an additional sample synthesised to explain deviation of the data for Pr-based composition.*

In $Ba_{0.5}La_{0.5}CoO_3$, the oxygen sites are fully occupied and the ionic radii difference between Ba and La is small enough ($\Delta R_{Ba,La} = 0.26$ Å). The result is a random A-site occupation of Ba and La with equal proportions and all oxygen sites being

equivalent. Annealing in Ar introduces more oxygen vacancies and favours A-site ordering. Hence, Ba and La sites are no longer crystallographically equivalent and two alternating A-site layers $Ba-O$ and $La-O(v_o)$ are formed. Therefore, when oxygen vacancies are formed upon reduction, the compound undergoes phase transformation into a layered structure in which oxygen site occupancy in the Co and Ba layers is close to 1 and oxygen in the La layer is depleted.

The unit cell volume increase linearly with the Ln ionic radius, R_{Ln}, as shown in Figure 4 (pseudo-cubic unit cell parameters are additionally presented in Figure S7). The general trend of decreasing unit cell volume along the lanthanide series is also seen in *a* and *c* unit cell parameters. However, the *b* parameter does not present a monotonic dependency and its total change as the Ln radius changes (excluding Pr-based compound) does not exceed 1%. Furthermore, the degree of orthorhombic distortion follows the trend of decreasing R_{Ln}. $BaPrCo_2O_{6-\delta}$ deviates from the general trend – this composition was synthesised using the same route as other samples, but the mass of the prepared sample was much higher than that of the others. Therefore, the access to oxygen during the synthesis may have been limited. If the specimen was slightly reduced, it could exhibit a smaller unit cell. To verify it, we synthesised another specimen using a smaller amount of powder. The result is inserted in Fig. 4a, b and d as open symbol marked as Pr_{ox}. One can see that this new specimen fits the trend much better indicating that the slightest change in oxidation conditions, heavily affects the structural properties. The refinement of specimen Pr_{ox} yielded tetragonal P4/mmm structure, however the analysis relied on XRD data only thus the orthorhombic distortion cannot be excluded.

The ratio between the O3b and O3a site occupancy, which in the tetragonal structure should be equal to one (both sites are equivalent), decreases with increasing orthorhombic distortion. PND refinements show that the ratio decreases from 0.98 for orthorhombic $BaLaCo_2O_{6-\delta}$ to 0.095 for $BaTbO_2O_{6-\delta}$ (*cf.* Figure 4.e). This trend was also observed directly from SR-PXD diffractograms as the low-angle peaks associated with the orthorhombic phase are more pronounced in compositions with smaller lanthanides (*cf.* Figures 3 and S2-8).

Transmission Electron Microscopy

Cation ordering and superstructures were studied by TEM. Grains oriented along the main pseudocubic zone axis were selected for all compositions. In all cases, the composition determined by EDS was close to nominal and no additional elements were detected. The results of the EDS studies are summarised in SI (*cf.* SI Table S9 and Figure S8).

TEM images of typical $BaLaCo_2O_{6-\delta}$ and $BaPrCo_2O_{6-\delta}$ crystal grains and the corresponding Selected Area Electron Diffraction (SAED) patterns are presented in Figure 5. Additional examples of TEM results, including $BaNdCo_2O_{6-\delta}$ and $BaGdCo_2O_{6-\delta}$, are given in Figures S9-12. In all cases, the strong diffraction spots can be indexed according to the structure of the single-perovskite cubic unit cell. However, weaker spots can be noticed halfway between the strong spots, certifying a doubling of the lattice parameter. The indexing of the diffraction spots in Figure 5.b refers to the $\{001\}_p$ interplanar distance in a single perovskite (a_p=3.9 Å measured in BLCO), pointing also to the diffraction spots which correspond to a structure with a double lattice parameter, $2a_p$ (roughly 7.8 Å). By carefully inspecting the outermost diffraction spots (e.g. the 10 0 0 spots), one can notice their splitting into two fine spots. The separation distance indicates a 1% variation of the interplanar distance, which perfectly fits the values of the b and c lattice parameters refined from the XRD pattern for the orthorhombic structure of BLCO. The spots splitting indicates that the area selected for electron diffraction within the analysed grain contains two kinds of orthorhombic domains rotated at 90° to each other around the common a-axis. SAED of $BaNdCo_2O_{6-\delta}$ and $Ba^{160}GdCo_2O_{6-\delta}$ also revealed superstructure spots from an orthorhombic superstructure in agreement with the powder diffraction data

Both $BaLaCo_2O_{6-\delta}$ (Fig. 5.a,b.) and $BaPrCo_2O_{6-\delta}$ (Fig. 5.c-e.), showed structural domains with different TEM contrast, arising from their different relative orientation with respect to the electron beam. The SAED patterns in Figure 5.d and e have been recorded from two neighbouring areas corresponding to the two contrast areas denoted with A and B on the micrograph in Figure 5.c. The size of the two circular areas corresponds to the trace of the smallest selecting aperture

used to obtain the two SAED patterns. Both diffraction patterns contain rows of diffraction spots of alternating strong/weak intensity. These rows are disposed vertically in Figure 5.d and horizontally in Figure 5.e. The two patterns can be indexed in agreement with the double-perovskite orthorhombic structure of $BaPrCo_2O_{6-\delta}$ (space group *Pmmm*) with a=3.86 Å, b=7.70 Å and c=7.5 Å.

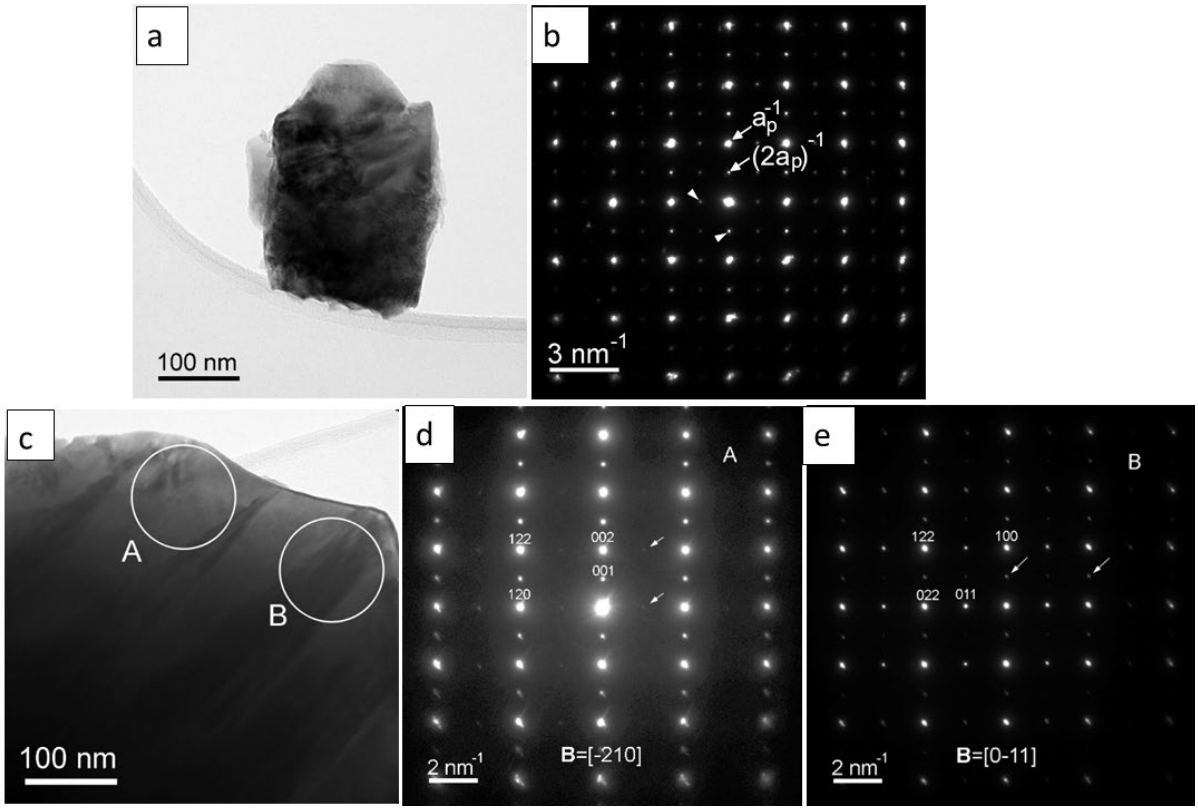

Figure 5. Examples of grains analysed by TEM: $BaLaCo_2O_{6-\delta}$ micrograph (a) and corresponding SAED pattern (b); $BaPrCo_2O_{6-\delta}$ micrograph (c) and SAED patterns of zones A (d) and B (e). Zones axes and indices are according to an orthorhombic double perovskite unit cell.

The presence of the weak hkl diffraction spots, with l odd, in Figure 5.d is due to the doubling of the c lattice parameter with respect to the cubic perovskite. Similarly, the weak hkl spots, with k and l odds, in Figure 5.e are due to the doubling of the b and c lattice parameters. The two types of domains observed in the same grain correspond to two different crystal orientations according to the **B**= [-210] and **B**= [0-11] zone axes, sharing the (122) family of planes. The crystallographic relation between the A and B domains is $[-210]_A \,||\, [0-11]_B$, $(001)_A \,||\, (100)_B$. An additional set of faint spots is observed (pointed by tilted arrows) in the SAED patterns of A and B zones. These spots are not allowed and do not actually belong to the diffraction patterns along the two mentioned zone axes.

However, they are visible in the two patterns due to the imperfect area selection inside a single domain because of the selecting aperture being slightly larger than the size of the domains.

The A-site ordering of Ba and the lanthanides has been studied further by two techniques: contrast analysis of the HRTEM micrographs ($BaLaCo_2O_{6-\delta}$ and $BaPrCo_2O_{6-\delta}$), and STEM combined with EELS analysis ($BaLaCo_2O_{6-\delta}$, $BaPrCo_2O_{6-\delta}$, $BaNdCo_2O_{6-\delta}$ and $BaGdCo_2O_{6-\delta}$). HRTEM contrast analysis is given for $BaLaCo_2O_{6-\delta}$ in Figure 6. Observing the periodicity doubling in the real space is not quite straightforward. However, the intensity line profiles measured along the

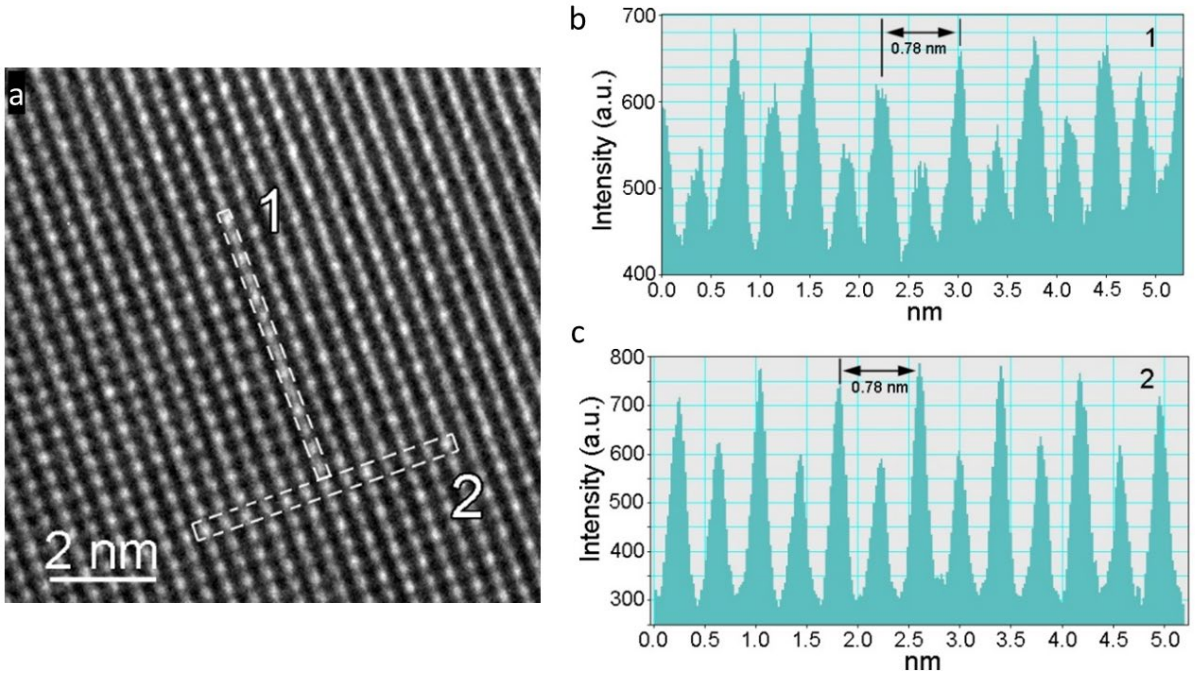

Figure 6. HRTEM brightness intensity analysis: (a) micrograph of selected area in $BaLaCo_2O_{6-\delta}$ grain (left) and the two image intensity profiles measured along line 1 and 2 (right).

rows of bright dots (cf. Figure 6.a) reveal that their brightness is not constant along the rows for $BaLaCo_2O_{6-\delta}$, but it shows a periodic amplitude variation, with a 7.8 Å period, twice the cubic perovskite lattice parameter (3.9 Å). In the case of $BaLaCo_2O_{6-\delta}$ the brightness variations can be observed in two perpendicular directions with a similar periodicity. Analogous observations have been made for the other studied compositions (e.g. SI Figure S16). This corresponds well with the structural parameters obtained from Rietveld refinement and indicates A-site ordering of Ba-Ln cations along the c-axis and a preference for oxygen vacancy

ordering along the b-axis. However, caution should be taken when only simple intensity modulation is analysed.

The intensity modulation of the HRTEM micrographs was further investigated and associated with the atomic structure by simulating the HRTEM patterns with the multislice technique. The patterns in Figure 7 were simulated as a function of thickness and defocus based on the structural model from Rietveld refinement with PND and SR-PXD data for $BaPrCo_2O_{6-\delta}$. Two matrices of HRTEM patterns were simulated along two zone axes: **B**= [-210] (Figure 7.a) and **B**= [0-11] (Figure 7.b).

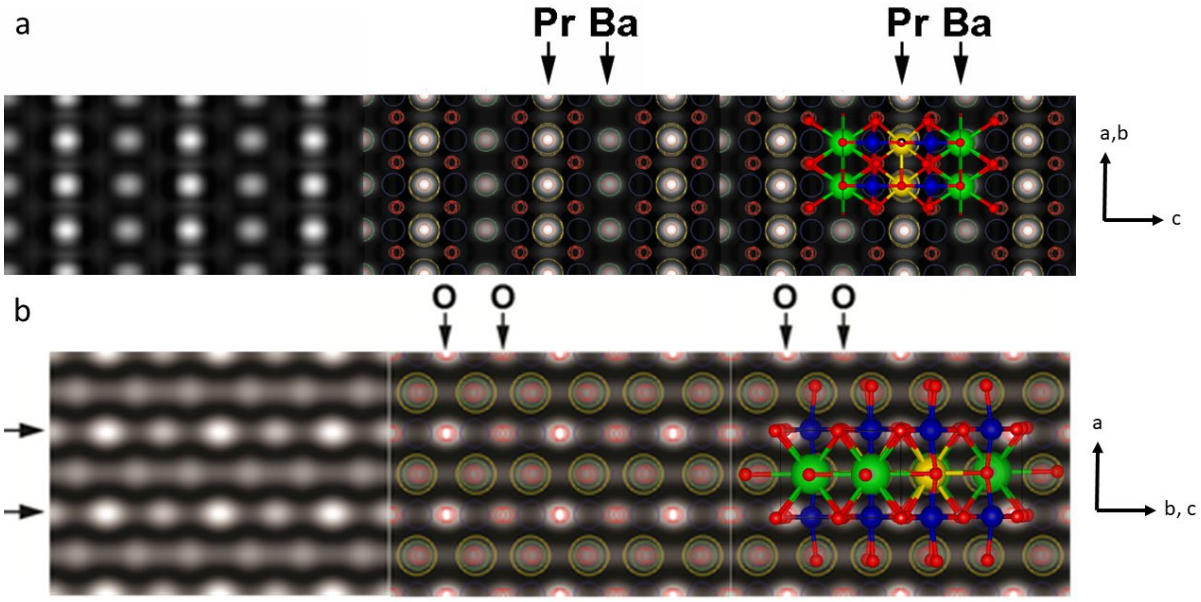

*Figure 7. HRTEM pattern simulation fit for $BaPrCo_2O_{6-\delta}$ along **B**= [-210] zone axis (a) and the simulation along **B**= [0-11] zone axis (b). The HRTEM simulation is presented in a raw form (left), with atomic positions overlay (middle) and with unit cell ball-stick model overlay (right). The crystal axes are given on the far right for orientation. Colours of the ions are yellow-Pr, green-Ba, blue-Co and red-O.*

The process of simulation and selection of the best fit is described in detail in the SI (cf. SI Figures S13-14). For the **B**=[-210] orientation, after analysing the phase contrast in the simulated images with the experimental one (*cf.* Figure 7.a), overlapping the structural model and the simulated image demonstrates that the intensity modulation attributed to the lattice parameter doubling along [001] corresponds to the Ba/Pr cationic ordering. Similarly, for the B=[0-11] orientation (Figure 7.b), overlapping the structural model and the simulated image

demonstrates that the observed intensity modulation indicating the doubling of the lattice parameter along [011] is associated with the oxygen positions, pointing to a process of oxygen vacancies ordering. This can be easily understood analysing the atomic structural model used for HRTEM simulation (shown as the overlay in Figure 7.b) rotated in [100] orientation. The Ba/Pr cation ordering on alternating {001} planes cannot explain the intensity modulation observed along [110]. However, the partial occupation of the oxygen positions and the ordering of the resulting vacancies on alternating {010} planes along the b-axis, leads to {011} planes containing oxygen vacancies alternating with fully occupied {011} planes. This corresponds to a period doubling along the b-axis, but also along the [011] direction as noticed on the experimental SAED pattern and HRTEM images in [0-11] zone axis orientation (*cf.* Figures 5.c-e). The double-headed arrows between the structural models in Figure 7.b point to the {011} oxygen planes containing vacancies. The distance between these planes is 0.54 nm, as measured on the experimental HRTEM images. The [0-11] orientation of the analysed grain is among the few orientations which allow evidencing the presence and ordering of the oxygen vacancies along the b and c axes. In this orientation, the atomic columns containing only oxygen are aligned parallel to the electron beam while the ordered vacancies are not masked by other atoms.

The results of STEM measurements and their corresponding EELS elemental maps are shown in Figure 8, while the EELS spectra, which served for element identification, are given in the SI Figure S16. Mapping of the elements on a small section of the STEM images was performed, confirming elemental composition of $BaLaCo_2O_{6-\delta}$, $BaNdCo_2O_{6-\delta}$, and $BaGdCo_2O_{6-\delta}$ (*cf.* Figures 8.a, 8.b and 8.c, respectively). Chemical ordering of Ba-Ln along the c-axis can be clearly seen from the obtained maps. In $BaLaCo_2O_{6-\delta}$, however, Ba and La are only partially ordered in separate A-sites (the model of unit cell derived from TEM results is given in SI Figure S10). All other studied compositions are fully A-site ordered. To confirm the consistency with the PND and SR-PXD data, a new Rietveld refinement was performed where 25% of the Ba sites were occupied by La and vice versa in both the orthorhombic and tetragonal phase. The R-factor, R_{wp} decreased slightly to 5.55

% compared to 5.60% for the models with fully ordered cation sublattice. The powder diffraction data are thus consistent with the TEM results.

In the case of $BaLaCo_2O_{6-\delta}$, apart from the Ba/La ordering along the c axis revealed by EELS mapping, on a careful analysis of the HAADF contrast in the STEM image (Fig. 8a) one can notice also the doubling of the lattice parameter along the perpendicular direction, as well (the b axis). The double-period pattern along b is associated with the HAADF contrast of the Co-containing columns along the imaged [100] zone axis (Co-O columns, actually). As the HAADF contrast is not sensitive to light elements such as oxygen, the observed double period contrast is generated by the Co3+ ions situated in two alternating atomic positions along [010] in the case of the orthorhombic phase of $BaLaCo_2O_{6-\delta}$ (denoted Co1 and Co2 in Table S2 in Supplementary information). We therefore conclude that the analysed $BaLaCo_2O_{6-\delta}$ grain showing double periodicity along two reciprocally perpendicular pseudocubic directions belongs to the orthorhombic phase refined from the SR-PXD patterns.

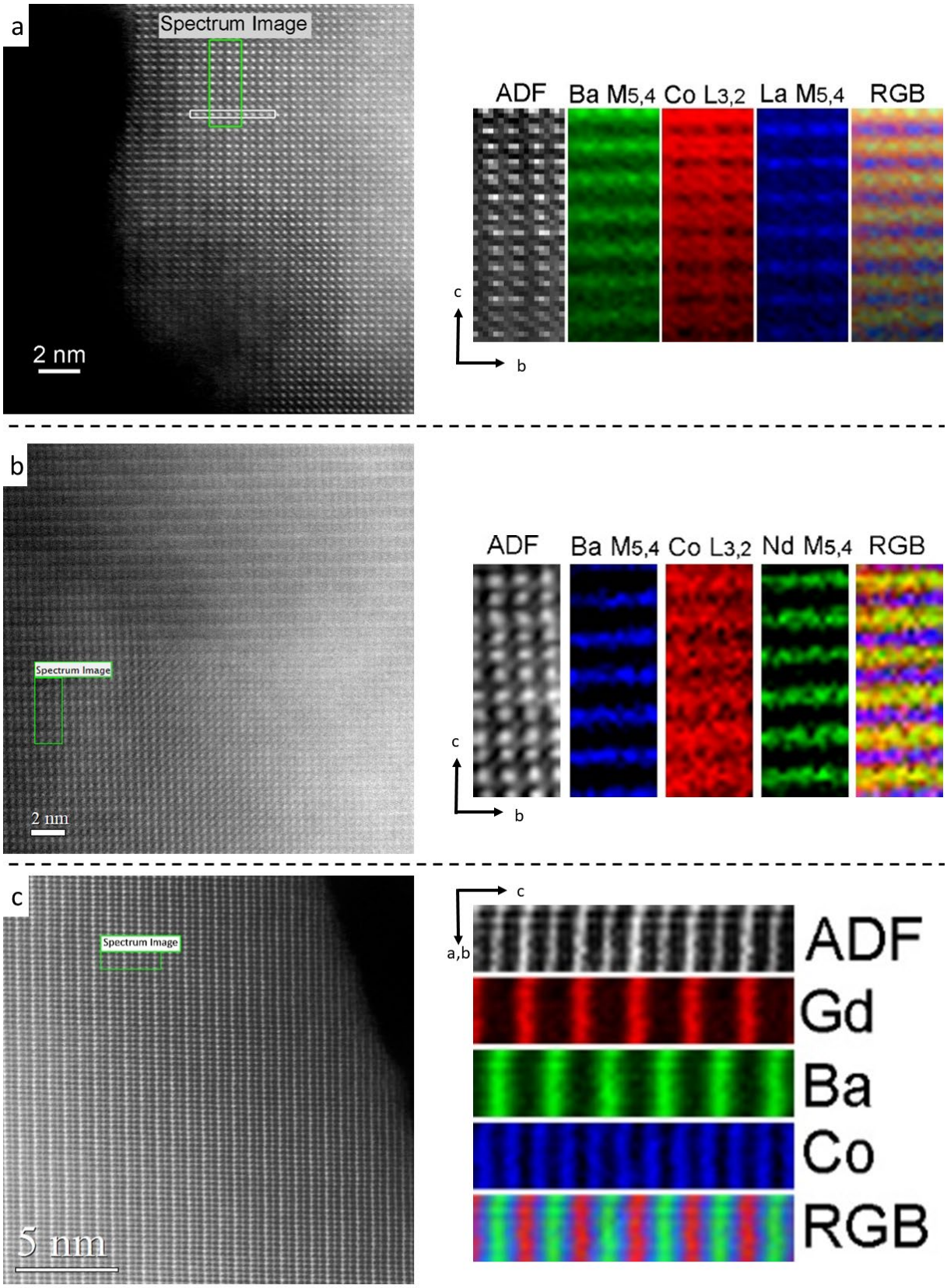

Figure 8. STEM micrograph of the area selected for EELS analysis and the EELS map of (a) $BaLaCo_2O_{6-\delta}$, (b) $BaNdCo_2O_{6-\delta}$, (c) $BaGdCo_2O_{6-\delta}$.

Oxygen non-stoichiometry

Oxygen non-stoichiometry was calculated from averaged Co oxidation state, obtained by iodometric titration, matching the results from PND measurements within the uncertainty. A detailed comparison of the results is presented in SI Table 9.

Figure 9 presents the results of oxidation studies. The data from iodometric titration were used as the starting point for the thermogravimetric studies of oxygen under-stoichiometry. The highest initial average Co oxidation state is observed for cubic $Ba_{0.5}La_{0.5}CoO_{3-\delta}$. For the double perovskites, the average Co oxidation state plotted as a function of Ln ionic radius (*cf.* Figure 9.a) shows that the oxidation state decreases with a decreasing radius. As expected, the double perovskite $BaLaCo_2O_{6-\delta}$ exhibit a lower oxidation state than its cubic counterpart. The comparison of the average cobalt oxidation state and its correspondent oxygen non-stoichiometry as a function of temperature for $Ba_{0.5}La_{0.5}CoO_{3-\delta}$ and $BaLaCo_2O_{6-\delta}$ are presented in Figure 9.b. The cubic structure is the most stable for the La-based composition, however, during the measurement of $BaLaCo_2O_{6-\delta}$ there are no signs of oxidation which could lead to formation the cubic structure.

Titration revealed that indeed one $BaPrCo_2O_{6-\delta}$ specimen is reduced, and one is oxidised thus confirming the coherence between the oxidation state and cell parameters given in Figure 4.

Figure 9 b, c and d depict that the onset temperatures for oxygen release are between 250 and 350 °C. The exact temperature varies with composition and no clear trend can be seen with changing Ln radius. Above the onset temperature, the oxygen non-stoichiometry decreases almost linearly with increasing temperature. Similar behaviour is observed for cooling (dashed lines). Comparison of thermal evolution of Co oxidation state measured upon cooling for all studied compositions, except $BaTbCo_2O_{6-\delta}$ and $BaDyCo_2O_{6-\delta}$, is shown in Figure 9.d. For all studied compositions, the temperature dependencies of cobalt oxidation state share the same features – a monotonic decrease with increasing temperature above the onset temperature.

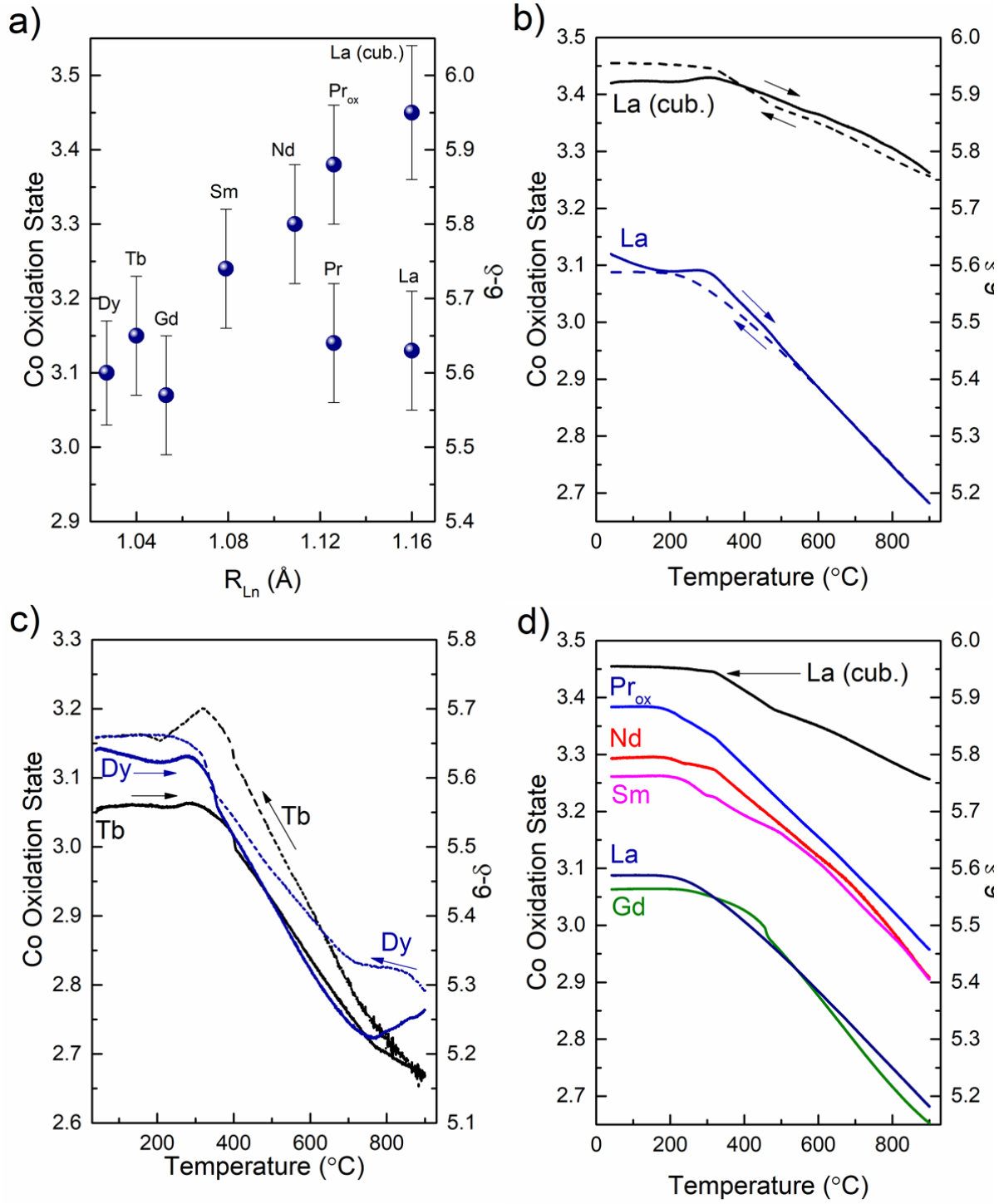

Figure 9. Results of oxidation studies: (a) Average Co oxidation state and oxygen non-stoichiometry as a function of ionic radius, determined by iodometric titration at room temperature. (b) Typical evolution of the average cobalt oxidation state and oxygen non-stoichiometry as a function of temperature exemplified for cubic $Ba_{0.5}La_{0.5}CoO_{3-\delta}$ and $BaLaCo_2O_{6-\delta}$ double perovskite determined by thermogravimetry; (c) two compositions with double perovskite structure showing atypical behaviour $BaDyCo_2O_{6-\delta}$ and $BaTbCo_2O_{6-\delta}$; (d) comparison of different BLnCOs measured upon cooling. The arrows indicate heating and cooling steps of measurement cycle.

Taskin et al. [15] measured oxygen ions diffusion coefficient in monocrystals of $BaGdCo_2O_{6-\delta}$ showing that the coefficient decreases from $D \approx 10^{-5}$ cm^2s^{-1} at 575 °C to $D \approx 3*10^{-8}$ cm^2s^{-1} at 250 °C. On this basis one may estimate the effective diffusion length of oxygen ions. Root mean square displacement R calculated for three-dimensional diffusion and time interval within which the temperature in the experiment is changed by 1 °C (t = 30 s, $R = \sqrt{6Dt}$) yields 300 μm and 6 μm respectively at 575 °C and 250 °C. The SEM measurements of powder samples showed that typical sizes of crystal grains are between 2 and 10 μm (cf. SI Figure S21). This means that, with the assumption that D of compounds from this study is within the same orders of magnitude as the one measured by Taskin et al. [15], that at 300°C and above the specimens should be in equilibrium with the surrounding atmosphere and the measurement represents the actual oxidation thermodynamics. A similar conclusion can be drawn from the study of $BaNdCo_2O_{6-\delta}$ by Aksenova et al. [32], where two experiments were performed, one with 2K/min cooling rate and the other with 3 hour equilibration at a set of temperatures. Both experiments yielded the same values, therefore, confirming that the TG experiment represents the equilibrium oxygen non-stoichiometry above the onset temperature. Below 300°C, depending on the sample microstructure, the oxygen ions exchanged at the surface may not have enough time to migrate within the whole volume of the grain, which makes the case limited by kinetics.

Water uptake and surface adsorption

Figure 10 presents the water uptake for all investigated BLnCOs measured by thermogravimetry in synthetic air at 300°C. $BaLaCo_2O_{6-\delta}$ and $BaGdCo_2O_{6-\delta}$ showed significant water uptake after two hours of exposure to water vapour, 0.016 and 0.021 wt. %, respectively, while smaller uptake of 0.004 wt. % is observed for $BaDyCo_2O_{6-\delta}$. To compare the effect of A-site ordering, the water uptake was also measured in cubic $Ba_{0.5}La_{0.5}CoO_3$.

The comparison between La-based compounds (Figure 10.b) indicates that the ordered structure exhibits four times larger uptake than the disordered phase. The weight gain is slow, and not apparently reversible upon changing the atmosphere back to dry air, as would be expected in isothermal hydration/dehydration [33–35].

Formation of protonic defects is a result of either hydration or hydrogenation, and is expected to scale with the concentration of oxygen vacancies or electron holes, respectively [35–37]. Both depend on the average Co oxidation state, while no correlation between the water uptake and Co-oxidation state is seen. Therefore, other factors seem to govern the stability of protons in BLnCOs. Post-TG XRD measurements revealed no formation of secondary phases (*cf.* SI Figure S21), and TEM of $BaLaCo_2O_{6-\delta}$ showed no formation of amorphous phases on the surface of crystal grains (*cf.* SI Figure S17) either. The slow weight gain could be a result of hydration imposing structural changes that in turn affect the oxidation thermodynamics. The result will be a partial hydration and oxidation process where a new red-ox equilibrium is reached after the hydration process. This explanation will be investigated further in future work.

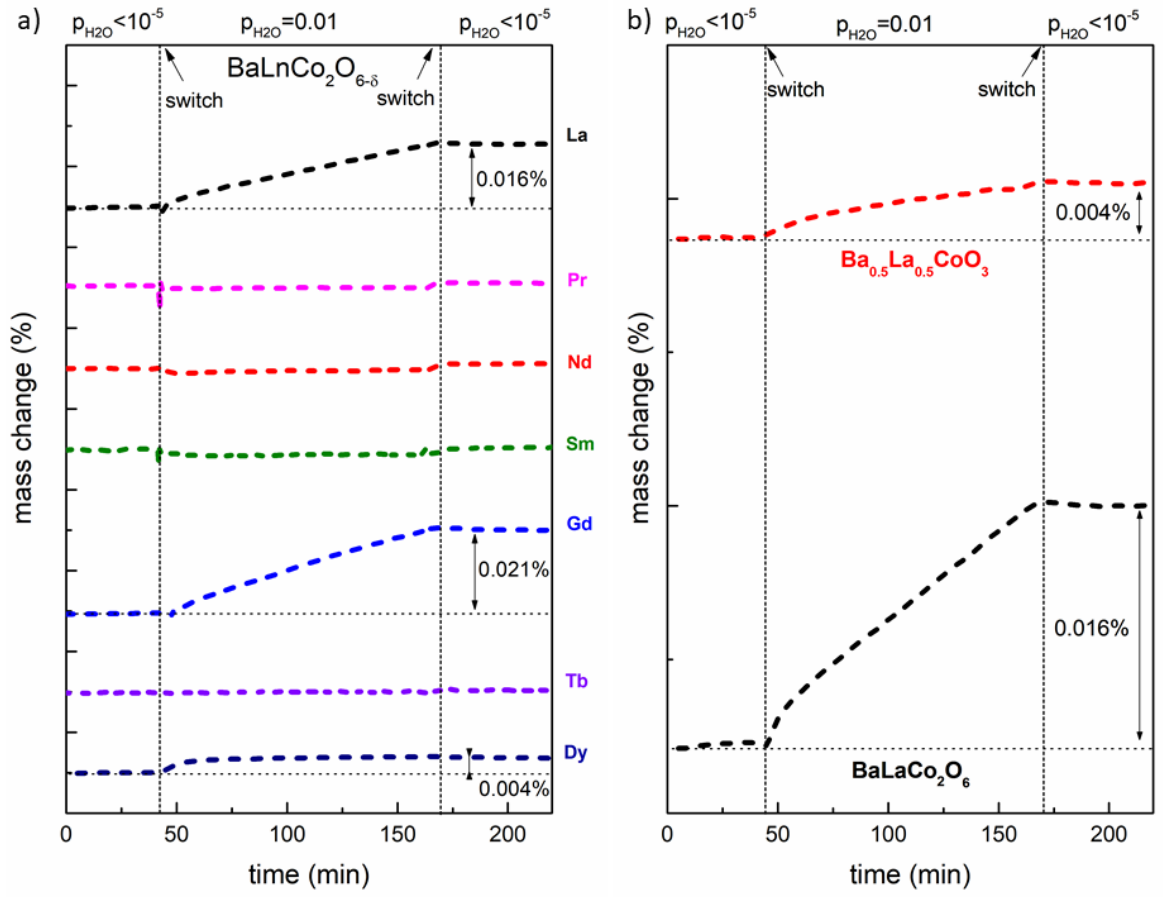

Figure 10. Water uptake in (a) $BaLnCo_2O_{6-\delta}$ (Ln = La, Pr, Nd, Sm, Gd, Dy, Tb) measured at 300°C and (b) comparison between water uptake in $Ba_{0.5}La_{0.5}CoO_3$ and $BaLaCo_2O_{6-\delta}$.

To further study the interaction of water with barium lanthanide cobaltites, water adsorption studies were performed. Such studies may show the affinity of the surface to react with water, which also is of central interest for the application as electrode material. Water vapour adsorption studies were performed at room temperature on all compositions (Figure 11). In most cases, the measurement represents type II isotherm according to IUPAC classification, whereas the sorption isotherm of the sample containing dysprosium is close to the type V [38]. Observed shapes of the isotherms suggest a multilayer adsorption process [39]. A different type of isotherm seen in the case of the sample with dysprosium indicates that this sample is more porous than the others. This corresponds well with the results of SEM microstructure studies and the specific surface area measured by BET method, which revealed that the area is low for all specimens (0.2-0.6 cm^2/g, *cf.* Table S11).

Two different quantitative indexes can be extracted from adsorption isotherms to express the hydrophilicity or hydrophobicity of material [40,41]. The water adsorption capacity (expressed in standard ccm of water per g of the specimen) reflects the total amount of water that can be stored at the surface. This parameter strongly depends on specimen microstructure, i.e. grain size, specific surface area, pore size, shape, and distribution. So that, the water adsorption capacity cannot serve as a direct indicator of the hydrophilicity of the material, but it rather should be considered as a measure of its porosity. The second parameter called α is a chemical activity of water vapour (in this case the relative pressure) at which half of the total water capacity is reached. The main advantage of using this parameter is that it is normalised ($0 < \alpha < 1$) and independent of the value of water adsorption capacity. It is also independent of specific surface area and thus to some extent sample morphology. The higher the α the more hydrophobic the material is. The water capacity and α parameter have been plotted as a function of Ln ionic radius respectively in Figures 11.e and 11.f.

The capacity of water adsorption in the studied BLnCOs follows a U-shape across the series of lanthanides. The highest capacity is observed in both polymorphs of La-based compound and $BaDyCo_2O_{6-\delta}$, while the other samples show quite similar

values of water adsorption capacity (between 0.22 and 0.35 ccm/g). The values of α parameter (Fig. 11 f) in double perovskites is close to or above 0.5 whereas for the cubic $Ba_{0.5}La_{0.5}CoO_3$ it equals 0.32. Therefore, cubic $Ba_{0.5}La_{0.5}CoO_3$ may be considered as hydrophilic, while the others are either neutral or weakly hydrophobic. Hydrophobicity of rare earth oxides was reported earlier by Azimi et al. [42]. The α values are not correlated with the water uptake results observed with the TG experiments. Even though surface adsorption processes can differ considerably at room temperature and at 300 °C, some parallels can be drawn. While the enthalpy of chemisorption is relatively small (minus few to minus tens of kJ/mol), the enthalpy of physisorption of the first layer of adsorbed water is as large as -100 kJ/mol [43]. In that sense the first layer of physisorbed water should form at 300 °C and parameters representing hydrophobicity of the surface should be somewhat connected to the formation of the first layer too. Moreover, the TG water uptake experiment is a combination of bulk and surface water uptake. However, the parameters obtained from water absorption experiment do not correlate with TG water uptake. This in combination with the absence of crystalline and amorphous secondary phases after the TG experiment (cf. SI Figures S17 and S21) indicates that water uptake is a bulk process related to the layered structure of the perovskite lattice and is characteristic uniquely to the presence of La or Gd in the lattice.

Bulk water uptake in two of the BLnCO compositions cannot be solely related to Ln radius, Co oxidation state or oxygen non-stoichiometry, which are the materials properties investigated in this work. Further studies related to electronic or structural acid-base properties will be pursued to elaborate the intriguing behaviour of some of these double perovskite cobaltites in wet conditions.

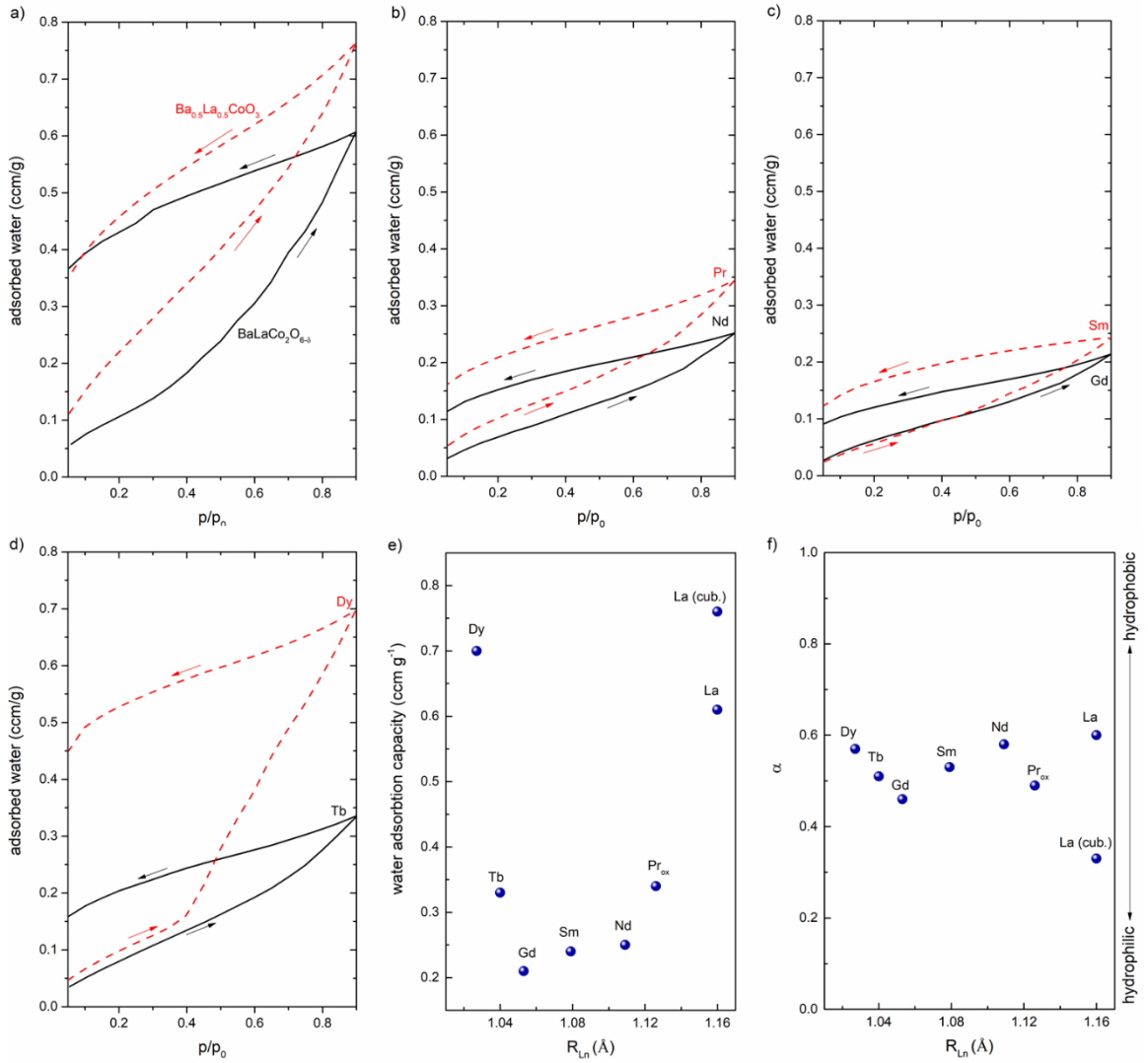

Figure 11. Water adsorption studies results. Isotherms at room temperature of (a) $Ba_{0.5}La_{0.5}CoO_3$ and $BaLaCo_2O_{6-\delta}$, (b) $BaPrCo_2O_{6-\delta}$ and $BaNdCo_2O_{6-\delta}$, (c) $BaSmCo_2O_{6-\delta}$ and $BaGdCo_2O_{6-\delta}$, (d) $BaTbCo_2O_{6-\delta}$ and $BaDyCo_2O_{6-\delta}$, (e) total volume of water adsorbed at the highest vapour pressure and (f) α parameter plotted as a function of R_{Ln} radius. Arrows indicate the direction of the process: to the right – sorption, to the left – desorption.

4. Conclusions

All the investigated perovskites with general formula $BaLnCo_2O_{6-\delta}$ are found to be either two phase systems with major orthorhombic and minor tetragonal structures (Ln = La, Sm), or single phase orthorhombic (Ln = Pr, Nd, Gd, Tb, Dy). The alternating Ba-Ln layers were directly observed by TEM via EELS elemental mapping, and orthorhombic ordering on the oxygen sublattice was refined from

SR-PXD and PND and observed by TEM. For Ln = La, Nd and Gd, orthorhombic oxygen ordering was shown by electron diffraction and the periodicity of contrast modulation in the HR-TEM pictures. Oxygen vacancies ordering could also be directly observed in the TEM micrograph when the oxygen sites were oriented parallel to the beam. The structural analysis revealed that the unit cell parameters a and c, and the degree of oxygen ordering along the b-axis depend on the Ln ionic radius, while the b-parameter was found to be independent of Ln radius.

Water uptake at 300°C in humidified atmosphere was observed in $BaLaCo_2O_{6-\delta}$ and $BaGdCo_2O_{6-\delta}$. A slight mass increase was observed in the disordered $Ba_{0.5}Ln_{0.5}CoO_{3-\delta}$ and the ordered $BaDyCo_2O_{6-\delta}$, what is correlated to high surface water adsorption for these compositions. The magnitude of surface water adsorption follows a U-shape across the investigated lanthanides as a function of ionic radius, with the highest adsorption for La and Tb. The four- to fivefold mass gain in wet atmosphere for $BaLaCo_2O_{6-\delta}$ and $BaGdCo_2O_{6-\delta}$ with respect to $Ba_{0.5}Ln_{0.5}CoO_{3-\delta}$ and $BaDyCo_2O_{6-\delta}$ combined with a lower surface adsorption of water for the former two suggest a bulk-related process. Bulk water uptake in two of the compositions cannot be related to the materials properties investigated in this work.

Acknowledgements

The research has been supported by the National Science Centre Poland (2016/22/Z/ST5/00691), the Spanish Government (PCIN-2017-125), and the Research Council of Norway (Grant nº 272797 "GoPHy MiCO") through the M-ERA.NET Joint Call 2016.

Funding from the Spanish Government (RTI2018-102161 and IJCI-2017-34110 grant) is kindly acknowledged.

The authors acknowledge the skilful assistance from the staff of the Swiss–Norwegian Beamline (SNBL), at the European Synchrotron Radiation Facility (ESRF), Grenoble, France. Dr Cheng Li is at POWGEN, SNS, Oak Ridge, US and Dr Chiu C. Tang at beamline I11 at Diamond, Didcot, UK are gratefully acknowledged for PND and SR-PXD measurements, respectively, of $BaGdCo_2O_{6-\delta}$.

SLW and AMG acknowledge the CERIC-ERIC Consortium for the access to experimental facilities and the financial support (No 20187079).

CG and MCI acknowledge the financial support from Romanian Ministry of Research and Innovation in the frame of the Core Program PN19-03.

SLW would like to express gratitude to Małgorzata Nadolska from Gdańsk University of Technology for support in surface measurements and analysis.

Contribution

SLW, MHS, CG, AMG and RS conceived, designed and supervised the research. SLW was the main contributor to the study, while RS conceptualised the study and was the main supervisor.

IS and MB synthesised the materials.

MHS was the main contributor responsible for structural studies and analysis. MG was responsible for XRD studies, while MHS for SR-PXD, PND and Rietveld refinement.

CG was the main contributor with respect to TEM studies and analysis. MCI did HRTEM simulations. TEM measurements of $BaGd^{160}Co_2O_{6-\delta}$ and cross-analysis with structural data from TOF-SIMS were performed by AEG.

AMG was the main contributor for thermal analysis, while IS did iodometric titration. SW performed water adsorption studies.

JMS, MG and TN are senior scientists whose contribution lied in a theoretical analysis of the results with respect to a broader scope of materials science, with solid state ionics in particular.

All authors contributed to writing the manuscript.

References

[1] R. Pelosato, G. Cordaro, D. Stucchi, C. Cristiani, G. Dotelli, Cobalt based layered perovskites as cathode material for intermediate temperature Solid Oxide Fuel Cells: A brief review, J. Power Sources. 298 (2015) 46–67. https://doi.org/10.1016/j.jpowsour.2015.08.034.

[2] S. Choi, C.J. Kucharczyk, Y. Liang, X. Zhang, I. Takeuchi, H.-I. Ji, S.M. Haile, Exceptional power density and stability at intermediate temperatures in protonic ceramic fuel cells, Nat. Energy. 3 (2018) 202–210. https://doi.org/10.1038/s41560-017-0085-9.

[3] E. Vøllestad, R. Strandbakke, M. Tarach, D. Catalán-Martínez, M.-L. Fontaine, D. Beeaff, D.R. Clark, J.M. Serra, T. Norby, Mixed proton and electron conducting double perovskite anodes for stable and efficient tubular proton ceramic electrolysers, Nat. Mater. 18 (2019) 752–759. https://doi.org/10.1038/s41563-019-0388-2.

[4] A. Løken, S. Ricote, S. Wachowski, Thermal and Chemical Expansion in Proton Ceramic Electrolytes and Compatible Electrodes, Crystals. 8 (2018) 365. https://doi.org/10.3390/cryst8090365.

[5] C. Bernuy-Lopez, L. Rioja-Monllor, T. Nakamura, S. Ricote, R. O'Hayre, K. Amezawa, M.-A. Einarsrud, T. Grande, Effect of Cation Ordering on the Performance and Chemical Stability of Layered Double Perovskite Cathodes, Materials (Basel). 11 (2018) 196. https://doi.org/10.3390/ma11020196.

[6] A. Grimaud, K.J. May, C.E. Carlton, Y.-L. Lee, M. Risch, W.T. Hong, J. Zhou, Y. Shao-Horn, Double perovskites as a family of highly active catalysts for oxygen evolution in alkaline solution, (2013). https://doi.org/10.1038/ncomms3439.

[7] R. Strandbakke, V.A. Cherepanov, A.Y. Zuev, D.S. Tsvetkov, C. Argirusis, G. Sourkouni, S. Prünte, T. Norby, Gd- and Pr-based double perovskite cobaltites as oxygen electrodes for proton ceramic fuel cells and electrolyser cells, Solid State Ionics. 278 (2015) 120–132. https://doi.org/10.1016/j.ssi.2015.05.014.

[8] M. Li, K. Chen, B. Hua, J. li Luo, W.D.A. Rickard, J. Li, J.T.S. Irvine, S.P. Jiang, Smart utilization of cobaltite-based double perovskite cathodes on barrier-layer-free zirconia electrolyte of solid oxide fuel cells, J. Mater. Chem. A. 4 (2016) 19019–19025. https://doi.org/10.1039/c6ta08396j.

[9] H. Téllez, J. Druce, Y.W. Ju, J. Kilner, T. Ishihara, Surface chemistry evolution in $LnBaCo_2O_{5+\delta}$ double perovskites for oxygen electrodes, Int. J. Hydrogen Energy. 39 (2014) 20856–20863. https://doi.org/10.1016/j.ijhydene.2014.06.102.

[10] I. Szpunar, S. Wachowski, T. Miruszewski, K. Dzierzgowski, K. Górnicka, T. Klimczuk, M.H. Sørby, M. Balaguer, J.M. Serra, R. Strandbakke, M. Gazda, A. Mielewczyk-Gryń, Electric and magnetic properties of lanthanum barium cobaltite, J. Am. Ceram. Soc. 103 (2020) 1809–1818. https://doi.org/10.1111/jace.16865.

[11] T. V. Aksenova, L.Y. Gavrilova, D.S. Tsvetkov, V.I. Voronin, V.A. Cherepanov, Crystal structure and physicochemical properties of layered perovskite-like phases $LnBaCo_2O_{5+\delta}$, Russ. J. Phys. Chem. A. 85 (2011) 427–432. https://doi.org/10.1134/S0036024411030022.

[12] G. Goupil, T. Delahaye, B. Sala, F. Lefebvre Joud, G. Gauthier, Selection and study of basic layered cobaltites as mixed ionic–electronic conductors for proton conducting fuel cells, Solid State Ionics. 263 (2014) 15–22. https://doi.org/10.1016/j.ssi.2014.04.022.

[13] a Maignan, C. Martin, D. Pelloquin, N. Nguyen, B. Raveau, Structural and Magnetic Studies of Ordered Oxygen-Deficient Perovskites $LnBaCo_2O_{5+\delta}$, Closely Related to the "112" Structure, J. Solid State Chem. 142 (1999) 247–260. https://doi.org/10.1006/jssc.1998.7934.

[14] E.-L. Rautama, V. Caignaert, P. Boullay, A.K. Kundu, V. Pralong, M. Karppinen, C. Ritter, B. Raveau, New Member of the "112" Family, $LaBaCo_2O_{5.5}$: Synthesis, Structure, and Magnetism, Chem. Mater. 21 (2009) 102–109. https://doi.org/10.1021/cm8021775.

[15] A.A. Taskin, A.N. Lavrov, Y. Ando, Achieving fast oxygen diffusion in perovskites by cation ordering, Appl. Phys. Lett. 86 (2005) 1–3. https://doi.org/10.1063/1.1864244.

[16] H. Andersen, K. Xu, D. Malyshkin, R. Strandbakke, A. Chatzitakis, A highly efficient electrocatalyst based on double perovskite cobaltites with

immense intrinsic catalytic activity for water oxidation, Chem. Commun. 56 (2020) 1030–1033. https://doi.org/10.1039/C9CC08765F.

[17] C. Duan, J. Tong, M. Shang, S. Nikodemski, M. Sanders, S. Ricote, A. Almansoori, R. OHayre, R. O'Hayre, Readily processed protonic ceramic fuel cells with high performance at low temperatures, Science. 349 (2015) 1321–1326. https://doi.org/10.1126/science.aab3987.

[18] D. Guan, J. Zhou, Z. Hu, W. Zhou, X. Xu, Y. Zhong, B. Liu, Y. Chen, M. Xu, H. Lin, C. Chen, J. Wang, Z. Shao, Searching General Sufficient-and-Necessary Conditions for Ultrafast Hydrogen-Evolving Electrocatalysis, Adv. Funct. Mater. 29 (2019) 1900704. https://doi.org/10.1002/adfm.201900704.

[19] A.L. Sednev, A.Y. Zuev, D.S. Tsvetkov, Oxygen Content and Thermodynamic Stability of $YBaCo_2O_{6-\delta}$ Double Perovskite , Adv. Mater. Sci. Eng. 2018 (2018) 1–6. https://doi.org/10.1155/2018/1205708.

[20] D.S. Tsvetkov, V.V. Sereda, A.Y. Zuev, Oxygen nonstoichiometry and defect structure of the double perovskite $GdBaCo_2O_{6-\delta}$, Solid State Ionics. 180 (2010) 1620–1625. https://doi.org/10.1016/j.ssi.2009.10.014.

[21] T. Norby, R. Strandbakke, M.H. Sørby, A. Mielewczyk–Gryń, S.L. Wachowski, J.M. Serra, Governing Principles in Hydration of Mixed Conducting Oxides, (2016). https://www.mn.uio.no/smn/english/research/projects/chemistry/GoPHyMiCO/ (accessed February 20, 2020).

[22] D. Poetzsch, R. Merkle, J. Maier, Proton conductivity in mixed-conducting BSFZ perovskite from thermogravimetric relaxation, Phys. Chem. Chem. Phys. 16 (2014) 16446–16453. https://doi.org/10.1039/C4CP00459K.

[23] V. Dyadkin, P. Pattison, V. Dmitriev, D. Chernyshov, A new multipurpose diffractometer PILATUS@SNBL, J. Synchrotron Radiat. 23 (2016) 825–829. https://doi.org/10.1107/S1600577516002411.

[24] P.M. Abdala, H. Mauroy, W. van Beek, A large-area CMOS detector for

high-energy synchrotron powder diffraction and total scattering experiments, J. Appl. Crystallogr. 47 (2014) 449–457. https://doi.org/10.1107/s1600576713034067.

[25] S.P. Thompson, J.E. Parker, J. Potter, T.P. Hill, A. Birt, T.M. Cobb, F. Yuan, C.C. Tang, Beamline I11 at Diamond: A new instrument for high resolution powder diffraction, Rev. Sci. Instrum. 80 (2009). https://doi.org/10.1063/1.3167217.

[26] B. Hauback, H. Fjellvåg, O. Steinsvoll, K. Johansson, O.T. Buset, J. Jørgensen, The high resolution Powder Neutron Diffractometer PUS at the JEEP II reactor at Kjeller in Norway, J. Neutron Res. 8 (2000) 215–232. https://doi.org/10.1080/10238160008200055.

[27] A. Huq, M. Kirkham, P.F. Peterson, J.P. Hodges, P.S. Whitfield, K. Page, T. Hűgle, E.B. Iverson, A. Parizzi, G. Rennich, POWGEN: rebuild of a third-generation powder diffractometer at the Spallation Neutron Source, J. Appl. Crystallogr. 52 (2019) 1189–1201. https://doi.org/10.1107/S160057671901121X.

[28] H.M. Rietveld, A profile refinement method for nuclear and magnetic structures, J. Appl. Crystallogr. 2 (1969) 65–71. https://doi.org/10.1107/S0021889869006558.

[29] A.A. Coelho, TOPAS and TOPAS-Academic: An optimization program integrating computer algebra and crystallographic objects written in C++: An, J. Appl. Crystallogr. 51 (2018) 210–218. https://doi.org/10.1107/S1600576718000183.

[30] K. Momma, F. Izumi, VESTA 3 for three-dimensional visualization of crystal, volumetric and morphology data, J. Appl. Crystallogr. 44 (2011) 1272–1276. https://doi.org/10.1107/S0021889811038970.

[31] P. Potapov, temDM - Software for TEM in Digital Micrograph, (2019). http://temdm.com/web/.

[32] T. V. Aksenova, L.Y. Gavrilova, A.A. Yaremchenko, V.A. Cherepanov, V. V.

Kharton, Oxygen nonstoichiometry, thermal expansion and high-temperature electrical properties of layered NdBaCo2O5+δand $SmBaCo_2O_{5+\delta}$, Mater. Res. Bull. 45 (2010) 1288–1292. https://doi.org/10.1016/j.materresbull.2010.05.004.

[33] A. Mielewczyk-Gryń, S. Wachowski, M. Prześniak-Welenc, K. Dzierzgowski, A. Regoutz, D. J. Payne, M. Gazda, D. Payne, M. Gazda, Water uptake analysis of the acceptor-doped lanthanum orthoniobates, J. Therm. Anal. Calorim. 6 (2019). https://doi.org/10.1007/s10973-019-08208-6.

[34] T. Miruszewski, K. Dzierzgowski, P. Winiarz, S. Wachowski, A. Mielewczyk-Gryń, M. Gazda, Structural properties and water uptake of STi1-xFexO3-x/2-δ, Materials. 13 (2020). https://doi.org/10.3390/ma13040965.

[35] R. Zohourian, R. Merkle, G. Raimondi, J. Maier, Mixed-conducting perovskites as cathode materials for protonic ceramic fuel cells: understanding the trends in proton uptake, Adv. Funct. Mater. 1801241 (2018) 1–10. https://doi.org/10.1002/adfm.201801241.

[36] D. Poetzsch, R. Merkle, J. Maier, Proton uptake in the H + -SOFC cathode material $Ba_{0.5}Sr_{0.5}Fe_{0.8}Zn_{0.2}O_{3-\delta}$: transition from hydration to hydrogenation with increasing oxygen partial pressure, Faraday Discuss. 182 (2015) 129–143. https://doi.org/10.1039/C5FD00013K.

[37] T.S. Bjørheim, M.F. Hoedl, R. Merkle, E.A. Kotomin, J. Maier, Proton, Hydroxide Ion, and Oxide Ion Affinities of Closed-Shell Oxides: Importance for the Hydration Reaction and Correlation to Electronic Structure, J. Phys. Chem. C. 124 (2020) 1277–1284. https://doi.org/10.1021/acs.jpcc.9b07570.

[38] Z. ALOthman, A Review: Fundamental Aspects of Silicate Mesoporous Materials, Materials. 5 (2012) 2874–2902. https://doi.org/10.3390/ma5122874.

[39] M. Khalfaoui, S. Knani, M.A. Hachicha, A. Ben Lamine, New theoretical expressions for the five adsorption type isotherms classified by BET based on statistical physics treatment, J. Colloid Interface Sci. 263 (2003) 350–

356. https://doi.org/10.1016/S0021-9797(03)00139-5.

[40] J. Canivet, A. Fateeva, Y. Guo, B. Coasne, D. Farrusseng, Water adsorption in MOFs: fundamentals and applications, Chem. Soc. Rev. 43 (2014) 5594–5617. https://doi.org/10.1039/C4CS00078A.

[41] J. Canivet, J. Bonnefoy, C. Daniel, A. Legrand, B. Coasne, D. Farrusseng, Structure–property relationships of water adsorption in metal–organic frameworks, New J. Chem. 38 (2014) 3102–3111. https://doi.org/10.1039/C4NJ00076E.

[42] G. Azimi, R. Dhiman, H.M. Kwon, A.T. Paxson, K.K. Varanasi, Hydrophobicity of rare-earth oxide ceramics, Nat. Mater. 12 (2013) 315–320. https://doi.org/10.1038/nmat3545.

[43] S. Raz, K. Sasaki, J. Maier, I. Riess, Characterization of adsorbed water layers on Y_2O_3-doped ZrO_2, Solid State Ionics. 143 (2001) 181–204. https://doi.org/10.1016/S0167-2738(01)00826-8.